

₁ Physics-Infused Reduced-Order Modeling for Analysis of
₂ Ablating Hypersonic Thermal Protection Systems

₃

₄ November 13, 2025

₅ **Abstract**

This work presents a *physics-infused reduced-order modeling* (PIROM) framework towards the design, analysis, and optimization of non-decomposing ablating hypersonic thermal protection systems (TPS). It is demonstrated via the modeling of transient thermo-ablative behavior of non-decomposing multi-layered hypersonic TPS. The PIROM architecture integrates a reduced-physics backbone, based on the lumped-capacitance model (LCM), with data-driven correction dynamics formulated via a coarse-graining approach rooted in the Mori-Zwanzig formalism. The LCM is coupled to a surface velocity model (SVM) to capture the recession of the ablating TPS as a function of the surface temperature. While the LCM and SVM capture the dominant physics of the ablating TPS response, the correction terms compensate for residual dynamics arising from higher-order non-linear interactions and heterogeneities across material layers. The PIROM consistently achieves errors below 1% for a wide range of extrapolative settings of design parameters involving time-and-space varying boundary conditions and SVM models, and improves by $x\%$ over the LCM alone. Moreover, the PIROM delivers online evaluations that are two orders of magnitude faster than the full-order model (FOM). These results demonstrate that PIRO effectively reconciles the trade-offs between accuracy, generalizability, and efficiency, providing a promising framework for optimizing multi-physical dynamical systems, such as TPS under diverse operating conditions.

₂₅ **1 Introduction**

₂₆ At hypersonic speeds, aerospace vehicles experience extreme aero-thermo-dynamic environments that require specialized thermal protection systems (TPS) to shield internal sub-
₂₇ structures, electronics, and possibly crew members from the intense aerodynamic heating.
₂₈

29 The TPS is often composed of ablating materials – a high-temperature capable fibrous
30 material injected with a resin that fills the pore network and strengthens the composite
31 [Amar2016](#). The TPS design promotes the exchange of mass through thermal and
32 chemical reactions (i.e., pyrolysis), effectively mitigating heat transfer to the sub-structures.

33 As a result, accurate prediction for the ablating TPS response under extreme hyper-
34 sonic heating becomes fundamental to ensuring survivability, performance, and safety of
35 hypersonic vehicles. Not only is it necessary to assess the performance of the thermal man-
36 agement systems, but also the shape changes of the vehicle’s outer surface induced by the
37 ablating material, and its impact on the aerodynamics, structural integrity, and controlla-
38 bility. Nonetheless, high-fidelity simulations of ablating TPS remains a formidable challenge
39 both theoretically and computationally.

40 Unfortunately, high-fidelity simulations of ablating TPS remains a formidable challenge
41 both theoretically and computationally.

42 On the theoretical side, the thermo-chemical reactions, coupled with the irregular pore
43 network structure, translate into simplifying assumptions to reduce non-linearities, and make
44 the resulting equations more amenable for engineering application and design analysis [x](#).
45 For instance, one of the most notable codes is the one-dimensional [CMA](#) code that was
46 developed by Aerotherm Corporation in the 1960s [Howard2015](#). Despite its practical use
47 in...

48 Another example is the CHarring Ablator Response (CHAR) ablation code, which ignores
49 elemental decompositions of the pyrolyzing gases, assumes the gases to be a mixture of perfect
50 gases in thermal equilibrium, and assumes no reaction or condensation with the porous
51 network [1].

52 [theoretically:](#)

53 [computationally:](#)

54 2 Modeling of Ablating Thermal Protection Systems

55 This section presents the problem of modeling a non-decomposing ablating TPS subjected to
56 extreme hypersonic heating. Two different but mathematically connected solution strategies
57 are provided: (1) a high-fidelity full-order model (FOM) based on a finite element method
58 (FEM), and (2) a low-fidelity reduced-physics model (RPM) based on a lumped capacitance
59 model (LCM) and a one-dimensional surface velocity model (SVM). The FOM is compu-
60 tationally expensive but provides the highest fidelity, while the RPM is computationally
61 efficeint but has low predictive fidelity; both models are amenable to high-dimensional de-
62 sign variables. The RPM is used in the subsequent sections for deriving the PIROM.

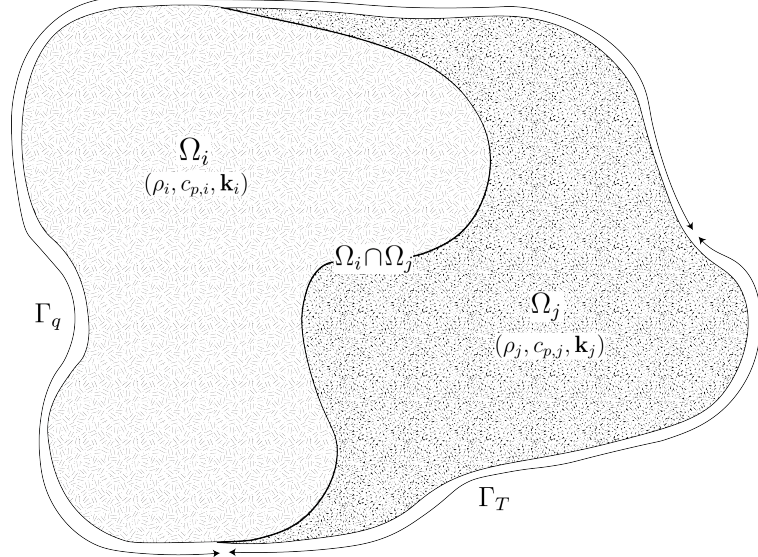


Figure 1: General domain Ω with prescribed Neumann and Dirichlet boundary conditions on Γ_q and Γ_T . Mesh displacement $w(x, t)$ occurs on the Γ_q boundary.

63 2.1 Governing Equations

64 The multi-physics for a non-decomposing ablating TPS involves the *energy equation* which
 65 models the transient heat conduction inside the TPS, and the *pseudo-elasticity equation*,
 66 which models the mesh motion due to surface recession. The governing PDEs for the ablating
 67 TPS are summarized in this section.

68 **Energy Equation** Consider a generic domain $\Omega \subset \mathbb{R}^d$, $d = 2$ or 3 , illustrated in Fig. 1. Let
 69 $\partial\Omega = \Gamma_q \cup \Gamma_T$ and $\Gamma_q \cap \Gamma_T = \emptyset$, where a Neumann $q_b(x, t)$ boundary condition is prescribed
 70 on the Γ_q boundary, and represents the surface exposed to the hypersonic boundary layer.
 71 The Dirichlet $T_b(x, t)$ boundary condition is prescribed on the boundary Γ_T . The TPS is
 72 divided into N non-overlapping components $\{\Omega_i\}_{i=1}^N$, as illustrated in Fig. 1 for $N = 2$.
 73 The i -th component Ω_i is associated with material properties $(\rho_i, c_{p,i}, \mathbf{k}_i)$, that are assumed
 74 to be continuous within one component, and can be discontinuous across two neighboring
 75 components.

76 The transient heat conduction is described by the energy equation,

$$\rho c_p \left(\frac{\partial T}{\partial t} + \tilde{\mathbf{v}}(x, t) \cdot \nabla T \right) - \nabla \cdot (\mathbf{k} \nabla T) = 0, \quad x \in \Omega \quad (1a)$$

$$-\mathbf{k} \nabla T \cdot \mathbf{n} = q_b(x, t), \quad x \in \Gamma_q \quad (1b)$$

$$T(x, t) = T_b(x, t), \quad x \in \Gamma_T \quad (1c)$$

$$T(x, 0) = T_0(x), \quad x \in \Omega \quad (1d)$$

77 where the density ρ is constant, while the heat capacity c_p and thermal conductivity $\mathbf{k} \in \mathbb{R}^{d \times d}$
78 may depend on temperature. In the order they appear, the terms in eq. (1a) include, the
79 unsteady energy storage, heat conduction, temperature advection due to mesh motion, and
80 source terms due to boundary conditions. The boundary conditions for the energy equation
81 includes Neumann eq. (1b) and Dirichlet eq. (1c) on Γ_T .

82 An Abirtrary Lagrangian-Eulerian (ALE) description is used to account for mesh motion
83 due to surface recession, where $\tilde{\mathbf{v}}(x, t)$ is the relative velocity of the material with respect to
84 the mesh,

$$\tilde{\mathbf{v}}(x, t) = \mathbf{v}_s(x, t) - \mathbf{v}_m(x, t) \quad (2)$$

85 where $\mathbf{v}_s(x, t)$ and $\mathbf{v}_m(x, t)$ are the physical material velocity and mesh velocity, respectively.
86 In this work, the physical material velocity is assumed to be zero, i.e., $\mathbf{v}_s(x, t) = \mathbf{0}$, and thus
87 the relative velocity is simply the negative of the mesh velocity, $\tilde{\mathbf{v}}(x, t) = -\mathbf{v}_m(x, t)$.

88 **Pseudo-Elasticity Equation** The mesh motion is described by the steady-state pseudo-
89 elasticity equation without body forces,

$$\nabla \cdot \boldsymbol{\sigma}(\mathbf{w}) = \mathbf{0}, \quad \forall t \in \mathcal{T}, \quad \mathbf{x} \in \Omega \quad (3a)$$

$$\mathbf{w}(\mathbf{x}, t) = \mathbf{w}_q(\mathbf{x}, t), \quad \forall t \in \mathcal{T}, \quad \mathbf{x} \in \Gamma_q \quad (3b)$$

$$\mathbf{w}(\mathbf{x}, t) = \mathbf{0}, \quad \forall t \in \mathcal{T}, \quad \mathbf{x} \notin \Gamma_q \quad (3c)$$

$$\mathbf{w}(\mathbf{x}, 0) = \mathbf{0}, \quad \forall \mathbf{x} \in \Omega \quad (3d)$$

90 where the stress tensor $\boldsymbol{\sigma}$ is related to the strain tensor $\boldsymbol{\epsilon}(\mathbf{w})$ through Hooke's law,

$$\boldsymbol{\sigma}(\mathbf{w}) = \mathbb{D} : \boldsymbol{\epsilon}(\mathbf{w})$$

91 where \mathbb{D} is the fourth-order positive definite elasticity tensor, and “ $:$ ” is the double con-
92 traction of the full-order tensor \mathbb{D} with the second-order tensor $\boldsymbol{\epsilon}$. The elasticity tensor
93 ordinarily possess a number of symmetries, effectively reducing the number of components

94 that describe it [2]. The symmetric strain tensor ϵ measures the deformation of the mesh
 95 due to displacements $\mathbf{w}(x, t)$, and is defined as,

$$\epsilon(\mathbf{w}) = \frac{1}{2} (\nabla \mathbf{w} + \nabla \mathbf{w}^\top)$$

96 The “material” properties for the mesh are chosen to tailor the mesh deformation, and need
 97 not represent the actual material being modeled [1].

98 For the pseudo-elasticity equations, the boundary conditions include prescribed displace-
 99 ments $\mathbf{w}_q(x, t)$ on the heated boundary Γ_q in eq. (3b), and zero displacements on the unheated
 100 boundaries in eq. (3c). The initial condition for the mesh displacements is zero in eq. (3d).
 101 Particularly, the surface velocity due to the ablating material is a function of the surface
 102 temperature $T_q(x, t)$ for $x \in \Gamma_q$ on the heated boundary. For the i -th material component,
 103 the mesh velocity on the heated boundary is imposed based on the following relation,

$$\hat{\mathbf{n}} \cdot \mathbf{v}_m(x, t) = f(T_q(x, t)), \quad x \in \Gamma_q \quad (4)$$

104 where $\hat{\mathbf{n}}$ is the unit normal vector on the heated boundary Γ_q , and f is a function obtained
 105 from tabulated data for the material, commonly referred to as a B' table [1]. The B' table
 106 provides a model for the recession velocity as a function of the surface temperature, and is
 107 pre-computed based on high-fidelity simulations of the ablation process for a one-dimensional
 108 slab of the material, and is independent of the TPS geometry. Provided the surface velocity,
 109 the boundary condition in eq. (5) for the mesh displacements are computed by integrating
 110 the surface velocity over time,

$$\mathbf{w}_q(x, t) = \int_0^t \mathbf{v}_m(x, \tau) d\tau \quad (5)$$

111 2.2 Full-Order Model: Finite-Element Method

112 To obtain the full-order numerical solution, the energy quation is spatially discretized using
 113 variational principles of the Discontinuous Galerkin (DG) method [3], while the pseudo-
 114 elasticity equation is discretized using the standard FEM; the result is a high-dimensional
 115 system of ODEs describing the temporal evolution of the temperature field and mesh dis-
 116 placements. Note that the choice of DG approach for the energy equation is mainly for
 117 *theoretical convenience* in the coarse-graining formulation, and is exclusively performed on
 118 the energy equation. The equivalence between DG and FEM is noted upon their convergence.

119 Consider a conforming mesh partition domain, where each element belongs to one and
 120 only one component. Denote the collection of all M elements as $\{E_i\}_{i=1}^M$. In an element E_i ,

¹²¹ its shared boundaries with another element E_j , Neumann BC, and Dirichlet BC are denoted
¹²² as e_{ij} , e_{iq} , and e_{iT} , respectively. Lastly, $|e|$ denotes the length ($n_d = 2$) or area ($n_d = 3$) of a
¹²³ component boundary e .

¹²⁴ For the i -th element, use a set of P trial functions, such as polynomials, to represent the
¹²⁵ temperature distribution,

$$T_i(x, t) = \sum_{l=1}^P \phi_l^i(x) u_l^i(t) \equiv \boldsymbol{\phi}_i^\top(x) \mathbf{u}_i(t), \quad i = 1, 2, \dots, M \quad (6)$$

¹²⁶ Without loss of generality, the trial functions are assumed to be orthogonal, so that,

$$\int_{E_i} \phi_l^i(x) \phi_k^i(x) d\Omega = 0, \quad l \neq k$$

¹²⁷ where δ_{lk} is the Kronecker delta function. Furthermore, for simplicity, choose $\phi_1^i = 1$. Thus,
¹²⁸ by orthogonality,

$$\int_{E_i} \phi_1^i(x) d\Omega = |E_i|, \quad \int_{E_i} \phi_k^i(x) d\Omega = 0, \quad k = 2, 3, \dots, P$$

¹²⁹ Under the choice of basis functions, u_1^i is simply the average temperature of element E_i ,
¹³⁰ denoted as \bar{u}_i .

¹³¹ By standard variational processes, e.g., [3], the element-wise governing equation is de-
¹³² noted as,

$$\mathbf{A}_i \dot{\mathbf{u}}_i = (\mathbf{B}_i + \mathbf{C}_i) \mathbf{u}_i + \sum_{j \in \mathcal{N}_i \cup \{T_b\}} (\mathbf{B}_{ij}^i \mathbf{u}_i + \mathbf{B}_{ij}^j \mathbf{u}_j) + \mathbf{f}_i(t), \quad \text{for } i = 1, 2, \dots, M \quad (7)$$

¹³³ which is collected as the following ODE for the all the elements in the mesh,

$$\mathbf{A}(\mathbf{u}) \dot{\mathbf{u}} = [\mathbf{B}(\mathbf{u}) + \mathbf{C}(\mathbf{u})] \mathbf{u} + \mathbf{f}(t) \quad (8)$$

¹³⁴ where $\mathbf{u} = [\mathbf{u}_1, \mathbf{u}_2, \dots, \mathbf{u}_M]^\top \in \mathbb{R}^{MP}$ includes all the DG variables, $\mathbf{f} \in \mathbb{R}^{MP}$ is the exter-
¹³⁵ nal forcing, and the system matrices \mathbf{A} , \mathbf{B} , and \mathbf{C} are the matrices due to heat capacity,
¹³⁶ heat conduction, and temperature advection due to mesh motion, respectively. A detailed
¹³⁷ derivation of eqs. (7) and (8) and their matrices is provided in Appendix A.

¹³⁸ **2.3 Reduced-Physics Model**

¹³⁹ The RPM for predicting the response of the ablating TPS consists of two components: (1)
¹⁴⁰ the *lumped-capacitance model* (LCM), and (2) the *surface velocity model* (SVM). The LCM is
¹⁴¹ described as a first-order system of ODEs for predicting the average temperatures inside the
¹⁴² components of the TPS, and provides a low-fidelity (under estimate) for the component's
¹⁴³ surface temperature. The SVM provides a relation between the surface temperature and
¹⁴⁴ the surface recession velocity based on pre-computed B' tables for the material, enabling the
¹⁴⁵ computation of one-dimensional surface displacements. The LCM and SVM are combined to
¹⁴⁶ define the RPM, providing low-fidelity estimates for the temperatures and surface recession
¹⁴⁷ of the ablating TPS.

¹⁴⁸ **2.3.1 Lumped Capacitance Model**

¹⁴⁹ A general form of the LCM is provided in this section; details regarding the derivation for
¹⁵⁰ the four-component TPS in Fig. 2 are provided in Appendix A. The LCM is a classical
¹⁵¹ physics-based low-order model for predicting the temporal variation of average temperature
¹⁵² in multiple interconnected components [4]. The LCM is derived at the component level from
¹⁵³ a point of view of energy conservation, and leads to the following system of ODEs for the
¹⁵⁴ average temperatures on the components,

$$\bar{\mathbf{A}}\dot{\bar{\mathbf{u}}} = \bar{\mathbf{B}}\bar{\mathbf{u}} + \bar{\mathbf{f}}(t) \quad (9)$$

¹⁵⁵ Where the states and inputs,

$$\bar{\mathbf{u}} = [\bar{u}_1, \bar{u}_2, \dots, \bar{u}_N]^\top \in \mathbb{R}^N, \quad \bar{\mathbf{f}} = [\bar{f}_1, \bar{f}_2, \dots, \bar{f}_N]^\top \in \mathbb{R}^N \quad (10)$$

¹⁵⁶ include the average temperatures $\bar{\mathbf{u}}$ and spatially-integrated inputs $\bar{\mathbf{f}}$ for the N components.
¹⁵⁷ For $i, j = 1, 2, \dots, N$ the (i, j) -th elements of the $\bar{\mathbf{A}} \in \mathbb{R}^{N \times N}$, $\bar{\mathbf{B}} \in \mathbb{R}^{N \times N}$, and $\bar{\mathbf{f}} \in \mathbb{R}^N$
¹⁵⁸ matrices are given by,

$$\bar{A}_i = \begin{cases} \int_{\Omega_i} \rho c_p d\Omega_i, & i = j \\ 0, & i \neq j \end{cases}, \quad \bar{B}_{ij} = \begin{cases} \sum_{j \in \mathcal{N}_i \cup \{T_b\}} \bar{B}_{ij}^i, & i = j \\ \bar{B}_{ij}^{(j)}, & i \neq j \end{cases}, \quad (11a)$$

$$\mathbf{f}_i = \begin{cases} |e_{iq}| \bar{q}_i + \frac{|e_{iT}|}{R_i} \bar{T}_i, & i = j \\ 0, & i \neq j \end{cases} \quad (11b)$$

¹⁵⁹ where,

$$\bar{q}_i = \frac{1}{|e_{iq}|} \int_{e_{iq}} q_b d e_{iq}, \quad \bar{T}_i = \frac{1}{|e_{iT}|} \int_{e_{iT}} T_b d e_{iT}, \quad \bar{B}_{ij}^i = -\frac{|e_{ij}|}{R_{ij}}, \quad \bar{B}_{ij}^j = \frac{|e_{ij}|}{R_{ij}} \quad (12)$$

¹⁶⁰ where R_{ij} is the equivalent thermal resistance between two neighboring components Ω_i and
¹⁶¹ Ω_j , and R_i is the thermal resistance between component Ω_i and the Dirichlet boundary.
¹⁶² The thermal resistances are computed based on the geometry and material properties of the
¹⁶³ components; details regarding their computation are provided in Appendix A.

¹⁶⁴ 2.3.2 Surface Velocity Model

¹⁶⁵ The displacement is assumed to be *one-dimensional* on the heated boundary Γ_q , i.e., the
¹⁶⁶ surface recedes only in the direction of the applied load, and occurs only for $\tilde{N} \leq N$ compo-
¹⁶⁷ nents. For example, in Fig. 2, the surface displacement on the heated boundary occurs only
¹⁶⁸ in the negative y -direction for the three components exposed to the hypersonic boundary
¹⁶⁹ layer; the fourth component is the substrate and does not ablate. Displacements along the
¹⁷⁰ x direction is small relative to displacements in the y direction, and are thus neglected.

¹⁷¹ For the i -th component, the SVM considered in this work takes the form,

$$\dot{\mathbf{w}} = \boldsymbol{\Xi} \bar{\mathbf{u}} - \tilde{\mathbf{f}} \quad (13)$$

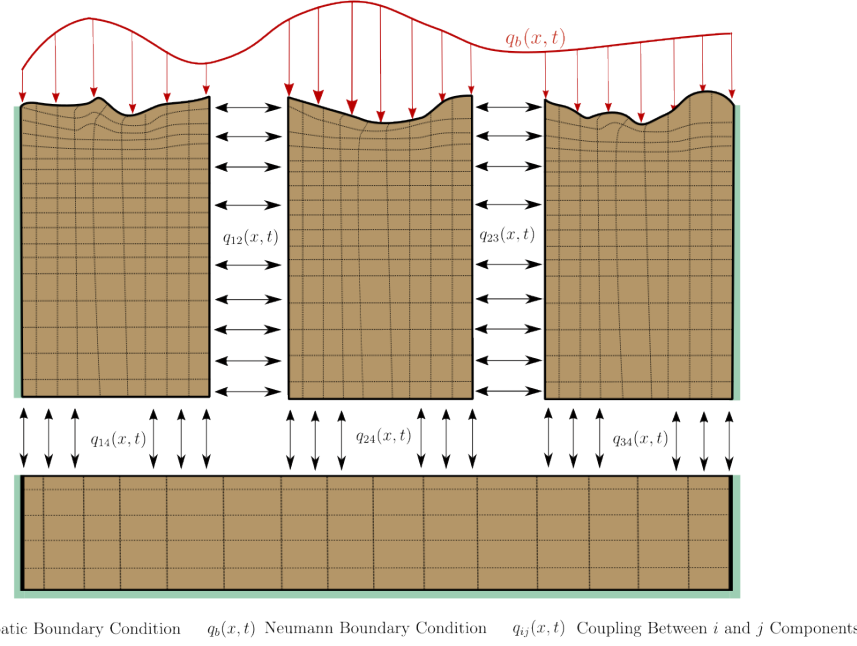
¹⁷² where $\boldsymbol{\Xi} = \text{diag}(\xi_1, \dots, \xi_{\tilde{N}})$ and $\tilde{\mathbf{f}} = (\xi_1 \bar{u}_{0,1}, \dots, \xi_{\tilde{N}} \bar{u}_{0,\tilde{N}})^\top$. The constants ξ_i are small
¹⁷³ material-dependent constants, determined from the B' table, and $\bar{u}_{0,i}$ is the constant initial
¹⁷⁴ temperature of the component. The SVM provides a relation between the surface tempera-
¹⁷⁵ ture and the surface recession velocity based on pre-computed B' tables for the material.

¹⁷⁶ 2.3.3 Coupled Reduced-Physics Model

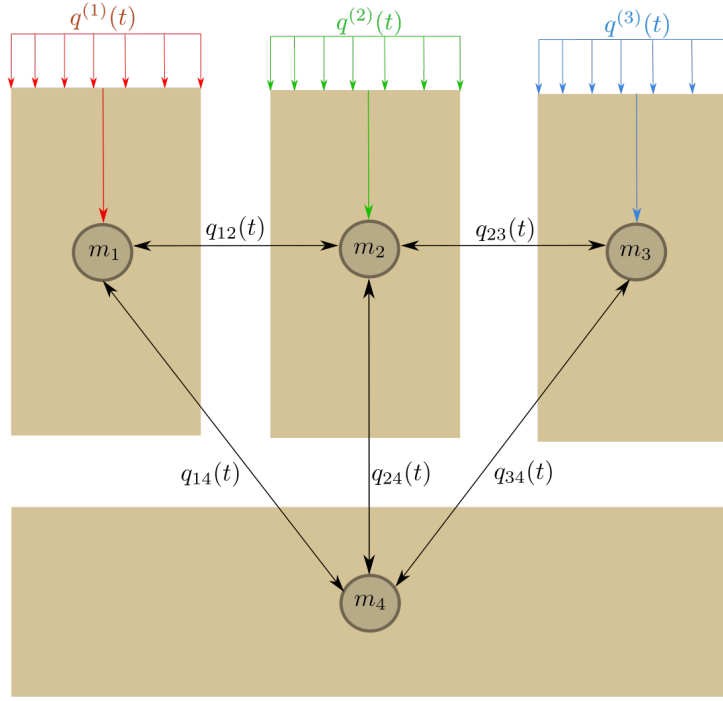
¹⁷⁷ The LCM and SVM are combined to define the RPM for predicting the thermo-ablative
¹⁷⁸ response of the TPS under hypersonic boundary layers. Specifically, the RPM is defined as
¹⁷⁹ the LCM as in eq. (9), where the *geometry-dependent matrices* $\bar{\mathbf{A}}$, $\bar{\mathbf{B}}$, and $\bar{\mathbf{f}}$ are updated at
¹⁸⁰ each time step based on the current surface displacements \mathbf{w} provided by the SVM. Assuming
¹⁸¹ the same material properties for the ablative components, the RPM is written as,

$$\mathcal{A}(\mathbf{s})\dot{\mathbf{s}} = \mathcal{B}(\mathbf{s})\mathbf{s} + \mathcal{F}(t) \quad (14)$$

¹⁸² where the state $\mathbf{s} = [\bar{\mathbf{u}}, \mathbf{w}]^\top \in \mathbb{R}^{N+\tilde{N}}$ includes the average temperatures for N components
¹⁸³ and the one-dimensional surface displacements for the \tilde{N} ablating components. The matrices



(a) TPS Decomposition



(b) Lumped Mass Representation

Figure 2: Partition of the TPS into three ablating and one non-ablating components with the corresponding lumped-mass representation.

184 are given as,

$$\mathcal{A} = \begin{bmatrix} \bar{\mathbf{A}}(\mathbf{w}) & \mathbf{0} \\ \mathbf{0} & \mathbf{I} \end{bmatrix}, \quad \mathcal{B}(\mathbf{s}) = \begin{bmatrix} \bar{\mathbf{B}}(\mathbf{w}) & \mathbf{0} \\ \Xi & \mathbf{0} \end{bmatrix}, \quad \mathcal{F}(t) = \begin{bmatrix} \bar{\mathbf{f}}(t) \\ -\tilde{\mathbf{f}} \end{bmatrix} \quad (15)$$

185 In the matrices $\bar{\mathbf{A}}$ and $\bar{\mathbf{B}}$, the surface displacements \mathbf{w} are used to define the dimensions for
186 the Ω_i component used in eqs. (11) and (12), thus effectively coupling the LCM and SVM.

187 2.4 Summary of Modeling Approaches

188 The FOM (i.e., DG-FEM) and RPM (i.e., LCM with SVM) are two different but mathemati-
189 cally connected solution strategies. Specifically, the LCM in eq. (9) not only resembles the
190 functional form of the DG model in eq. (8), but can be viewed as a special case of the latter,
191 where the mesh partition is extremely coarse, and the trial and test functions are piece-wise
192 constants. This removes all spatial variations within each component, and neglects advection
193 effects due to mesh motion.

194 For example, consider the case where each component Ω_i is treated as one single element,
195 and each element employs one constant basis function $\phi_i = 1$. The element-wise DG model
196 in eq. (7) simplifies into a scalar ODE,

$$\mathbf{A}^{(i)} = \bar{A}_i, \quad \mathbf{C}^{(i)} = 0, \quad \mathbf{B}_{ij}^{(i)} = -\sigma|e_{ij}|, \quad \mathbf{B}_{ij}^{(j)} = \sigma|e_{ij}|, \quad \mathbf{f}_i = |e_{iq}|\bar{q}_i + \sigma|e_{iT}|\bar{T}_i \quad (16)$$

197 Clearly, the LCM is a coarse zeroth-order DG model with the inverse of thermal resistance
198 chosen as the element-wise penalty factors. Or conversely, the DG model is a refined version
199 of LCM via hp -adaptation.

200 The FOM and RPM represent two extremes in the modeling fidelity and computational
201 cost spectrum. On one hand, the FOM is the most accurate but computationally expensive
202 to evaluate due to the fine mesh discretizations for both the temperature and displacement
203 fields, leading to possibly millions of state variables. On the other hand, the RPM considers
204 only the average temperature of the material from which one-dimensional surface displace-
205 ments are computed. This considerably reduces the computational cost, but sacrifices local
206 temperature information that are critical to properly capture higher-order effects due to
207 mesh motion and thermal gradients within each component. Thus, neither the FOM nor
208 the RPM is an universal approach for real-world analysis, design, and optimization tasks for
209 ablating TPS, where thousands of high-fidelity model evaluations may be necessary. This
210 issue motivates the development of the PIROM, which can achieve the fidelity of FOM at
211 a computational cost close to the RPM, while maintaining the generalizability to model

212 parameters.

213 3 Physics-Infused Reduced-Order Modeling

214 The formulation of PIROM for ablating TPS starts by connecting the FOM, i.e., the DG-
215 FEM, and the RPM, i.e., the LCM, via a coarse-graining procedure. This procedure pin-
216 points the missing dynamics in the LCM when compared to DG-FEM. Subsequently, the
217 Mori-Zwanzig (MZ) formalism is employed to determine the model form for the missing dy-
218 namics in PIROM. Lastly, the data-driven identification of the missing dynamics in PIROM
219 is presented.

220 3.1 Deriving the Reduced-Physics Model via Coarse-Graining

221 The subsequent coarse-graining formulation is performed on the DG-FEM in eq. (8) to derive
222 the LCM in eq. (9). This process constraints the trial function space of a full-order DG model
223 to a subset of piece-wise constants, so that the variables \mathbf{u} , matrices \mathbf{A} , \mathbf{B} , and \mathbf{C} , and forcing
224 vector \mathbf{f} are all approximated using a single state associated to the average temperature. Note
225 that the coarse-graining is exclusively performed to the thermal dynamics, as it is the surface
226 temperature that drives the one-dimensional surface recession via the SVM; hence, the SVM
227 is not included in this process.

228 3.1.1 Coarse-Graining of States

229 Consider a DG model as in eq. (8) for M elements and an LCM as in eq. (9) for N components;
230 clearly $M \gg N$. Let $\mathcal{V}_j = \{i | E_i \in \Omega_j\}$ be the indices of the elements belonging to the j -th
231 component, so $E_i \in \Omega_j$ for all $i \in \mathcal{V}_j$. The number of elements in the j -th component is $|\mathcal{V}_j|$.
232 The average temperature on Ω_j is,

$$\bar{u}_j = \frac{1}{|\Omega_j|} \sum_{i \in \mathcal{V}_j} \int_{E^{(i)}} \boldsymbol{\phi}^{(i)}(x)^T \mathbf{u}^{(i)} d\Omega = \frac{1}{|\Omega_j|} \sum_{i \in \mathcal{V}_j} |E_i| \boldsymbol{\varphi}_i^{j\top} \mathbf{u}^{(i)}, \quad j = 1, 2, \dots, N \quad (17)$$

233 where $|\Omega_j|$ and $|E_i|$ denote the area ($d = 2$) or volume ($d = 3$) of component j and element
234 i , respectively. The orthogonal basis functions are defined as $\boldsymbol{\varphi}_i^{j\top} = [1, 0, \dots, 0]^\top \in \mathbb{R}^P$.

235 Conversely, given the average temperatures of the N components, $\bar{\mathbf{u}}$, the states of an
236 arbitrary element E_i is written as,

$$\mathbf{u}^{(i)} = \sum_{k=1}^N \boldsymbol{\varphi}_i^k \bar{u}_k + \delta \mathbf{u}^{(i)}, \quad i = 1, 2, \dots, M \quad (18)$$

²³⁷ where $\varphi_i^k = 0$ if $i \notin \mathcal{V}_k$, and $\delta\mathbf{u}^{(i)}$ represents the deviation from the average temperature and
²³⁸ satisfies the orthogonality condition $\varphi_i^{k\top} \delta\mathbf{u}^{(i)} = 0$ for all k .

²³⁹ Equations eqs. (17) and (18) are combined and written in matrix form as,

$$\bar{\mathbf{u}} = \Phi^+ \mathbf{u}, \quad \mathbf{u} = \Phi \mathbf{u} + \delta\mathbf{u} \quad (19)$$

²⁴⁰ where $\Phi \in \mathbb{R}^{MP \times N}$ is a matrix of $M \times N$ blocks, with the (i, j) -th block as φ_i^j , $\Phi^+ \in \mathbb{R}^{N \times MP}$
²⁴¹ is the left inverse of Φ , with the (i, j) -th block as $\varphi_i^{j+} = \frac{|E_i|}{|\Omega_j|} \varphi_i^{j\top}$, and $\delta\mathbf{u}$ is the collection of
²⁴² deviations. By their definitions, $\Phi^+ \Phi = \mathbf{I}$ and $\Phi^+ \delta\mathbf{u} = \mathbf{0}$.

²⁴³ 3.1.2 Coarse-Graining of Dynamics

²⁴⁴ Next, consider a function of states in the form of $\mathbf{M}(\mathbf{u})\mathbf{g}(\mathbf{u})$, where $\mathbf{g} : \mathbb{R}^{MP} \rightarrow \mathbb{R}^{MP}$
²⁴⁵ is a vector-valued function, and $\mathbf{M} : \mathbb{R}^{MP} \rightarrow \mathbb{R}^{p \times MP}$ is a matrix-valued function with an
²⁴⁶ arbitrary dimension p . Define the projection matrix $\mathbf{P} = \Phi \Phi^+$ and the projection operator
²⁴⁷ \mathcal{P} as,

$$\begin{aligned} \mathcal{P} [\mathbf{M}(\mathbf{u})\mathbf{g}(\mathbf{u})] &= \mathbf{M}(\mathbf{P}\mathbf{u})\mathbf{g}(\mathbf{P}\mathbf{u}) \\ &= \mathbf{M}(\Phi\bar{\mathbf{u}})\mathbf{g}(\Phi\bar{\mathbf{u}}) \end{aligned} \quad (20)$$

²⁴⁸ so that the resulting function depends only on the average temperatures $\bar{\mathbf{u}}$. Correspondingly,
²⁴⁹ the residual operator $\mathcal{Q} = \mathcal{I} - \mathcal{P}$, and $\mathcal{Q}[\mathbf{M}(\mathbf{u})\mathbf{g}(\mathbf{u})] = \mathbf{M}(\mathbf{u})\mathbf{g}(\mathbf{u}) - \mathbf{M}(\Phi\bar{\mathbf{u}})\mathbf{g}(\Phi\bar{\mathbf{u}})$. When
²⁵⁰ the function is not separable, the projection operator is simply defined as $\mathcal{P}[\mathbf{g}(\mathbf{u})] = \mathbf{g}(\mathbf{P}\mathbf{u})$.

²⁵¹ Subsequently, the operators defined above are applied to coarse-grain the dynamics. First,
²⁵² write the DG-FEM in eq. (8) as,

$$\dot{\mathbf{u}} = \mathbf{A}(\mathbf{u})^{-1} \mathbf{B}(\mathbf{u}) \mathbf{u} + \mathbf{A}(\mathbf{u})^{-1} \mathbf{C}(\mathbf{u}) \mathbf{u} + \mathbf{A}(\mathbf{u})^{-1} \mathbf{f}(t) \quad (21)$$

²⁵³ and multiply both sides by Φ^+ to obtain,

$$\Phi^+ \dot{\mathbf{u}} = \Phi^+ (\Phi \dot{\bar{\mathbf{u}}} + \delta \dot{\mathbf{u}}) = \dot{\bar{\mathbf{u}}} = \Phi^+ \mathbf{r}(\mathbf{u}, t) \quad (22)$$

²⁵⁴ Apply the projection operator \mathcal{P} and the residual operator \mathcal{Q} to the right-hand side to obtain,

$$\dot{\bar{\mathbf{u}}} = \mathcal{P} [\Phi^+ \mathbf{r}(\mathbf{u}, t)] + \mathcal{Q} [\Phi^+ \mathbf{r}(\mathbf{u}, t)] \equiv \mathbf{r}^{(1)}(\mathbf{u}, t) + \mathbf{r}^{(2)}(\mathbf{u}, t) \quad (23)$$

²⁵⁵ where $\mathbf{r}^{(1)}(\mathbf{u}, t)$ is resolved dynamics that depends on $\bar{\mathbf{u}}$ only, and $\mathbf{r}^{(2)}(\mathbf{u}, t)$ is the un-resolved
²⁵⁶ or residual dynamics. Detailed derivations and analysis of $\mathbf{r}^{(1)}(\mathbf{u}, t)$ and $\mathbf{r}^{(2)}(\mathbf{u}, t)$ can be

257 found in the Appendix.

258 It follows from Ref. [8] that the resolved dynamics is exactly the LCM, where the ad-
259 vection term reduces to zero, i.e., $\bar{\mathbf{C}}(\bar{\mathbf{u}}) = \mathbf{0}$ as shown in the Appendix. Using the notation
260 from eq. (9), it follows that,

$$\begin{aligned}\mathbf{r}^{(1)}(\mathbf{u}, t) &= \bar{\mathbf{A}}(\bar{\mathbf{u}})^{-1} \bar{\mathbf{B}}(\bar{\mathbf{u}}) \bar{\mathbf{u}} + \bar{\mathbf{A}}(\bar{\mathbf{u}})^{-1} \bar{\mathbf{C}}(\bar{\mathbf{u}}) \bar{\mathbf{u}} + \bar{\mathbf{A}}(\bar{\mathbf{u}})^{-1} \bar{\mathbf{f}}(\bar{\mathbf{u}}) \\ &= \bar{\mathbf{A}}(\bar{\mathbf{u}})^{-1} \bar{\mathbf{B}}(\bar{\mathbf{u}}) \bar{\mathbf{u}} + \bar{\mathbf{A}}(\bar{\mathbf{u}})^{-1} \bar{\mathbf{f}}(t)\end{aligned}\quad (24)$$

261 where the following relations hold,

$$\bar{\mathbf{A}}(\bar{\mathbf{u}}) = \mathbf{W} (\Phi^+ \mathbf{A} (\Phi \bar{\mathbf{u}})^{-1} \Phi)^{-1} \quad \bar{\mathbf{C}}(\bar{\mathbf{u}}) = \mathbf{0} \quad (25a)$$

$$\bar{\mathbf{B}}(\bar{\mathbf{u}}) = \mathbf{W} \Phi^+ \mathbf{B} (\Phi \bar{\mathbf{u}}) \Phi \quad \bar{\mathbf{f}}(t) = \mathbf{W} \Phi^+ \mathbf{f} \quad (25b)$$

262 where $\mathbf{W} \in \mathbb{R}^{N \times N}$ is a diagonal matrix with the i -th element as $[\mathbf{W}]_{ii} = |\mathcal{V}_k|$ if $i \in \mathcal{V}_k$.

263 The examination of the second residual term $\mathbf{r}^{(2)}(\mathbf{u}, t)$ in eq. (23) is shown in the Appendix,
264 and demonstrates that the physical sources of missing dynamics in the LCM include: the
265 approximation of non-uniform temperature within each component as a constant, and the
266 elimination of the advection term due to coarse-graining. In sum, the above results not
267 only show that the LCM is a result of coarse-graining of the full-order DG-FEM, but also
268 reveal the discrepancies between the LCM and the DG-FEM. These discrepancies propagate
269 into the SVM, which as a result of the averaging in the LCM formulation, under-predicts
270 the surface recession rates. In the subsequent section, the discrepancies in the LCM are
271 corrected to formulate the PIROM.

272 3.2 Physics-Infusion Via Mori-Zwanzig Formalism

273 The Mori-Zwanzig (MZ) formalism is an operator-projection technique used to derive ROMs
274 for high-dimensional dynamical systems, especially in statistical mechanics and fluid dynam-
275 ics [5, 6, 7]. It provides an exact reformulation of a high-dimensional Markovian dynamical
276 system, into a low-dimensional observable non-Markovian dynamical system. The proposed
277 ROM is subsequently developed based on the approximation to the non-Markovian term in
278 the observable dynamics. Particularly, eq. (23) shows that the DG-FEM dynamics can be
279 decomposed into the resolved dynamics $\mathbf{r}^{(1)}(\mathbf{u}, t)$ and the orthogonal dynamics $\mathbf{r}^{(2)}(\mathbf{u}, t)$, in
280 the sense of $\mathcal{P}\mathbf{r}^{(2)} = 0$. In this case, the MZ formalism can be invoked to express the dynamics

281 $\bar{\mathbf{u}}$ in terms of $\bar{\mathbf{u}}$ alone as the projected Generalized Langevin Equation (GLE) [5, 6, 7],

$$\dot{\bar{\mathbf{u}}}(t) = \mathbf{r}^{(1)}(\bar{\mathbf{u}}, t) + \int_0^t \tilde{\kappa}(t, s, \bar{\mathbf{u}}) ds \quad (26)$$

282 where the first and second terms are referred to as the Markovian and non-Markovian terms,
283 respectively. The non-Markovian term accounts for the effects of past un-resolved states on
284 the current resolved states via a memory kernel $\tilde{\kappa}(t, s, \bar{\mathbf{u}})$, which in practice is computationally
285 expensive to evaluate.

286 **3.2.1 Markovian Reformulation**

287 This section details the formal derivation of the PIROM for the thermal dynamics, based on
288 approximations to the memory kernel. Specifically, the kernel $\tilde{\kappa}$ is examined via a leading-
289 order expansion, based on prior work [9]; this can be viewed as an analog of zeroth-order
290 holding in linear system theory with a sufficiently small time step. In this case, the memory
291 kernel is approximated as,

$$\tilde{\kappa}(t, s, \bar{\mathbf{u}}) \approx \mathbf{r}^{(1)}(\bar{\mathbf{u}}, t) \cdot \nabla_{\bar{\mathbf{u}}} \mathbf{r}^{(2)}(\Phi \bar{\mathbf{u}}, t) \quad (27)$$

292 Note that the terms in $\mathbf{r}^{(1)}$ have a common factor $\bar{\mathbf{A}}^{-1}$; this motivates the following heuristic
293 modification of the model form in eq. (26),

$$\dot{\bar{\mathbf{u}}} = \mathbf{r}^{(1)}(\bar{\mathbf{u}}, t) + \bar{\mathbf{A}}^{-1}(\bar{\mathbf{u}}) \int_0^t \kappa(t, s, \bar{\mathbf{u}}) ds \quad (28a)$$

$$\bar{\mathbf{A}}(\bar{\mathbf{u}}) \dot{\bar{\mathbf{u}}} = \bar{\mathbf{B}}(\bar{\mathbf{u}}) \bar{\mathbf{u}} + \bar{\mathbf{f}}(t) + \int_0^t \kappa(t, s, \bar{\mathbf{u}}) ds \quad (28b)$$

294 where the original kernel $\tilde{\kappa}$ is effectively normalized by $\bar{\mathbf{A}}^{-1}$. Intuitively, such choice of kernel
295 reduces its dependency on the averaged material properties, and simplifies the subsequent
296 design of model form.

297 Subsequently, the hidden states are introduced to “Markovianize” the system eq. (26).
298 In this manner, eq. (28b) is converted into a pure state-space model, with the functional
299 form of the LCM retained; since LCM is a physics-based model, then it encodes the phys-
300 ical information and retains explicit parametric dependence of the problem. Consider the
301 representation of the kernel as a finite sum of simpler functions, e.g., exponentials,

$$\kappa(t, s, \bar{\mathbf{u}}) = \sum_{j=1}^m \mathcal{K}_j(t, s, \bar{\mathbf{u}}) [\mathbf{p}_j + \mathbf{d}_j(\bar{\mathbf{u}})] \phi_j(s, \bar{\mathbf{u}}) \quad (29)$$

302 where,

$$\mathcal{K}_j(t, s, \bar{\mathbf{u}}) = e^{-\int_s^t (\lambda_j + e_j(\bar{\mathbf{u}})) d\tau}, \quad \phi_j(s, \bar{\mathbf{u}}) = \mathbf{q}_j^\top \bar{\mathbf{u}}(s) + \mathbf{g}_j(\bar{\mathbf{u}})^\top \bar{\mathbf{u}}(s) + \mathbf{r}_j^\top \bar{\mathbf{f}}(s) \quad (30)$$

303 with suitable coefficients $\mathbf{p}_j, \mathbf{d}_j, \mathbf{q}_j, \mathbf{g}_j, \mathbf{r}_j \in \mathbb{R}^N$ and decay rates $\lambda_j, e_j(\bar{\mathbf{u}}) > 0$, that need to
304 be identified from data.

305 Define the hidden states as,

$$\beta_j(t) = \int_0^t \mathcal{K}_j(s, \bar{\mathbf{u}}) \phi_j(s, \bar{\mathbf{u}}) ds \quad (31)$$

306 then through its differentiation with respect to time,

$$\dot{\beta}_j(t) = -[\lambda_j + e_j(\bar{\mathbf{u}})] \beta_j(t) + \mathbf{q}_j^\top \bar{\mathbf{u}}(t) + \mathbf{g}_j(\bar{\mathbf{u}})^\top \bar{\mathbf{u}}(t) + \mathbf{r}_j^\top \bar{\mathbf{f}}(t) \quad (32)$$

307 and the memory term becomes,

$$\int_0^t \boldsymbol{\kappa}(t, s, \bar{\mathbf{u}}) ds = \sum_{j=1}^m [\mathbf{p}_j + \mathbf{d}_j(\bar{\mathbf{u}})] \beta_j(t) \quad (33)$$

308 Then, eq. (28b) is recast as the extended Markovian system,

$$\bar{\mathbf{A}}(\bar{\mathbf{u}}) \dot{\bar{\mathbf{u}}} = \bar{\mathbf{B}}(\bar{\mathbf{u}}) \bar{\mathbf{u}} + [\mathbf{P} + \mathbf{D}(\bar{\mathbf{u}})] \boldsymbol{\beta} + \bar{\mathbf{f}}(t) \quad (34a)$$

$$\dot{\boldsymbol{\beta}} = [-\boldsymbol{\Lambda} + \mathbf{E}(\bar{\mathbf{u}})] \boldsymbol{\beta} + [\mathbf{Q} + \mathbf{G}(\bar{\mathbf{u}})] \bar{\mathbf{u}} + \mathbf{R} \bar{\mathbf{f}}(t) \quad (34b)$$

309 where,

$$\boldsymbol{\Lambda} = \text{diag}(\lambda_1, \lambda_2, \dots, \lambda_m) \in \mathbb{R}^{m \times m}, \quad \mathbf{P} = [\mathbf{p}_1, \mathbf{p}_2, \dots, \mathbf{p}_m] \in \mathbb{R}^{N \times m} \quad (35a)$$

$$\mathbf{D}(\bar{\mathbf{u}}) = [\mathbf{d}_1(\bar{\mathbf{u}}), \mathbf{d}_2(\bar{\mathbf{u}}), \dots, \mathbf{d}_m(\bar{\mathbf{u}})] \in \mathbb{R}^{N \times m}, \quad \mathbf{Q} = [\mathbf{q}_1, \mathbf{q}_2, \dots, \mathbf{q}_m] \in \mathbb{R}^{m \times N} \quad (35b)$$

$$\mathbf{G}(\bar{\mathbf{u}}) = [\mathbf{g}_1(\bar{\mathbf{u}}), \mathbf{g}_2(\bar{\mathbf{u}}), \dots, \mathbf{g}_m(\bar{\mathbf{u}})] \in \mathbb{R}^{m \times N}, \quad \mathbf{R} = [\mathbf{r}_1, \mathbf{r}_2, \dots, \mathbf{r}_m] \in \mathbb{R}^{m \times N} \quad (35c)$$

$$\mathbf{E}(\bar{\mathbf{u}}) = \text{diag}(e_1(\bar{\mathbf{u}}), e_2(\bar{\mathbf{u}}), \dots, e_m(\bar{\mathbf{u}})) \in \mathbb{R}^{m \times m} \quad (35d)$$

310 Since the hidden states $\boldsymbol{\beta}$ serve as the memory, their initial conditions are set to zero, i.e.,
311 $\boldsymbol{\beta}(t_0) = \mathbf{0}$, no memory at the beginning. The physics-infused model in eq. (34) retains the
312 structure of the LCM, while the hidden states account for missing physics through corrections
313 to the stiffness and advection matrices, as well as the forcing term.

³¹⁴ **3.2.2 Coupling with Surface Velocity Model**

³¹⁵ Provided the PIROM for the thermal dynamics in eq. (34), the last step in the formulation
³¹⁶ is to couple it with the SVM to account for the ablative surface recession.

³¹⁷ Lastly, denote the collection of resolved and hidden states as $\mathbf{y} = [\bar{\mathbf{u}}, \boldsymbol{\beta}]^T \in \mathbb{R}^{n_y}$ with
³¹⁸ $n_y = N + m$, then the proposed PIROM is summarized as,

$$\tilde{\mathbf{A}}\dot{\mathbf{y}} = [\tilde{\mathbf{B}} + \tilde{\mathbf{C}}] \mathbf{y} + \mathbf{H}\bar{\mathbf{f}}(t) \quad (36a)$$

$$\mathbf{z} = \mathbf{M}\mathbf{y} \quad (36b)$$

³¹⁹ where,

$$\tilde{\mathbf{A}} = \begin{bmatrix} \bar{\mathbf{A}}(\bar{\mathbf{u}}) & \mathbf{O} \\ \mathbf{O} & \mathbf{I} \end{bmatrix} \in \mathbb{R}^{n_y \times n_y}, \quad \tilde{\mathbf{B}} = \begin{bmatrix} \bar{\mathbf{B}}(\bar{\mathbf{u}}) & \mathbf{P} \\ \mathbf{Q} & -\boldsymbol{\Lambda} \end{bmatrix} \in \mathbb{R}^{n_y \times n_y}, \quad \tilde{\mathbf{C}} = \begin{bmatrix} \mathbf{0} & \mathbf{D}(\bar{\mathbf{u}}) \\ \mathbf{G}(\bar{\mathbf{u}}) & \mathbf{E}(\bar{\mathbf{u}}) \end{bmatrix} \in \mathbb{R}^{n_y \times n_y}, \quad (37a)$$

$$\mathbf{H} = \begin{bmatrix} \mathbf{I} \\ \mathbf{R} \end{bmatrix} \in \mathbb{R}^{n_y \times N}, \quad \mathbf{M} \in \mathbb{R}^{n_z \times n_y} \quad (37b)$$

³²⁰ In eq. (36), the terms $\bar{\mathbf{A}}$, $\bar{\mathbf{B}}$, and $\bar{\mathbf{f}}$ are the LCM terms. The collection of matrices,

$$\boldsymbol{\Theta} = \{\mathbf{P}, \mathbf{D}(\bar{\mathbf{u}}), \mathbf{G}(\bar{\mathbf{u}}), \boldsymbol{\Lambda}, \mathbf{E}(\bar{\mathbf{u}}), \mathbf{Q}, \mathbf{G}(\bar{\mathbf{u}}), \mathbf{R}, \mathbf{M}\}, \in \mathbb{R}^{n_\theta} \quad (38)$$

³²¹ are learnable parameters to capture the memory effects. Particularly, the matrices $\mathbf{P}, \boldsymbol{\Lambda}, \mathbf{Q}, \mathbf{R}$
³²² are constants that need to be identified from data, and account for the effects of coarse-
³²³ graining on the stiffness and forcing matrices. The matrices $\mathbf{D}(\bar{\mathbf{u}}), \mathbf{E}(\bar{\mathbf{u}}), \mathbf{G}(\bar{\mathbf{u}})$ are state-
³²⁴ dependent matrices, and account for the effects of coarse-graining on the advection matrix.
³²⁵ Leveraging the DG-FEM formula for the advection matrix in eq. (47c) in the Appendix, and
³²⁶ noting that the mesh displacements are functions of the ablating velocity as in eq. (4), the
³²⁷ state-dependent matrices for the i -th component are written as,

$$\mathbf{D}^{(i)}(\bar{\mathbf{u}}) \approx f^{(i)}(\bar{u}^{(i)})\mathbf{D}^{(i)}, \quad \mathbf{E}^{(i)}(\bar{\mathbf{u}}) \approx f^{(i)}(\bar{u}^{(i)})\mathbf{E}^{(i)}, \quad \mathbf{G}^{(i)}(\bar{\mathbf{u}}) \approx f^{(i)}(\bar{u}^{(i)})\mathbf{G}^{(i)} \quad (39)$$

³²⁸ where $f^{(i)}(\bar{u}^{(i)})$ is the surface recession velocity function in ?? for the i -th component,
³²⁹ and $\mathbf{D}^{(i)}, \mathbf{E}^{(i)}, \mathbf{G}^{(i)}$ are constant matrices to be identified from data. In eq. (36), \mathbf{M} is a
³³⁰ fully-populated matrix that extracts the observables, i.e., the surface temperatures, from
³³¹ the PIROM states \mathbf{y} . The PIROM incorporates explicit information on the temperature-
³³² dependent material properties through the LCM matrices, as well as the surface recession

³³³ velocity function through eq. (39). The next step is focused on identifying the unknown
³³⁴ parameters Θ characterizing the hidden dynamics.

³³⁵ 3.3 Learning the Hidden Dynamics from Data

³³⁶ The learning of the PIROM is achieved through a neural-ODE like approach [Chen2018](#).

³³⁷ For ease of presentation, consider the following compact form of the PIROM in eq. (36),

$$\mathcal{F}(\dot{\mathbf{y}}, \mathbf{y}; \boldsymbol{\xi}, \Theta) = \mathbf{0} \quad (40)$$

³³⁸ where $\boldsymbol{\xi}$ defines the parametrization of the problem, i.e., operating conditions, such as the
³³⁹ BC's, as well as the material properties. Consider a dataset of N_s high-fidelity trajectories
³⁴⁰ of observables over a time interval $[t_0, t_f]$,

$$\mathcal{D} = \left\{ \left(t_k, \mathbf{z}_{\text{HF}}^{(l)}(t_k), \boldsymbol{\xi}^{(l)} \right) \right\}_{l=1}^{N_s}, \quad k = 0, 1, \dots, K \quad (41)$$

³⁴¹ The learning problem is formulated as the following differentially-constrained problem,

$$\min_{\Theta} \quad \frac{1}{N_s} \sum_{l=1}^{N_s} \frac{1}{K} \sum_{k=0}^K \left\| \mathbf{z}_{\text{HF}}^{(l)}(t_k) - \mathbf{M}\mathbf{y}^{(l)}(t_k) \right\|_2^2 \quad (42a)$$

$$\text{s.t.} \quad \mathcal{F}(\dot{\mathbf{y}}^{(l)}, \mathbf{y}^{(l)}; \boldsymbol{\xi}^{(l)}, \Theta) = \mathbf{0}, \quad t \in [t_0, t_f], \quad l = 1, 2, \dots, N_s \quad (42b)$$

$$\mathbf{y}^{(l)}(t_0) = \mathbf{y}_0(\boldsymbol{\xi}^{(l)}), \quad l = 1, 2, \dots, N_s \quad (42c)$$

³⁴² 4 Application to Thermal Protection Systems

³⁴³ In this section,

³⁴⁴ 5 Conclusions

345 **A Technical Details**

346 This appendix presents the technical details of the PIROM framework applied to the TPS
347 ablation problem. The first section provides the mathematical details for the definition of
348 the DG-FEM. The second section follows the projection procedures from Ref. x, and demon-
349 strates the effects of coarse-graining on the advection matrix. The third section presents the
350 derivation of the LCM model from an energy-conservation perspective.

351 **A.1 Full-Order Model**

352 To obtain the full-order numerical solution, the governing equation is spatially discretized
353 using variational principles of Discontinuous Galerkin (DG) to result in a high-dimensional
354 system of ordinary differential equations (ODEs). The DG-FEM model is written in an
355 element-wise form, which is beneficial for subsequent derivations of the lower-order models.
356 Note that the choice of DG approach here is mainly for theoretical convenience in the sub-
357 sequent coarse-graining formulation. In the numerical results, the full-order TPS ablation
358 simulations is computed using standard FEM instead, and the equivalence between DG and
359 standard FEM is noted upon their convergence.

360 **A.1.1 Domain Discretization**

361 Consider a conforming mesh partition of the domain, as shown in Fig. DOMAIN, where each
362 element belongs to one and only one component. Denote the collection of all M elements
363 as $\{E_i\}_{i=1}^M$. To ease the description of the DG model, a graph structure is employed. The
364 elements are treated as vertices, the set of which is denoted $\mathcal{V} = \{m\}_{m=1}^M$. Two neighboring
365 elements, E_i and E_j , are connected by an edge (i, j) , and the shared boundary between them
366 is denoted e_{ij} . The collection of all edges are denoted \mathcal{E} , and \mathcal{G} is referred to as a graph.
367 In the graph, the edges are unidirected, meaning if $(i, j) \in \mathcal{E}$ then $(j, i) \in \mathcal{E}$. Furthermore,
368 denote the neighbors of the i -th element as $\mathcal{N}_i = \{j | (i, j) \in \mathcal{E}\}$. Lastly, for the ease of
369 notation, introduce two special indices: T for the boundary of an element that overlaps with
370 the Dirichlet boundary condition, and similarly q for the Neumann boundary condition.

³⁷¹ **A.1.2 Weak Form of Discontinuous Galerkin Method**

³⁷² Choosing appropriate basis functions ϕ_k and ϕ_l and using the Interior Penalty Galerkin
³⁷³ (IPG) scheme [3], the variational bilinear form for eq. (1a) is,

$$\sum_{i=1}^M a_{\epsilon,i}(\phi_k, \phi_l) = \sum_{i=1}^M L_i(\phi_k) \quad (43)$$

³⁷⁴ where ϵ is an user-specified parameter and,

$$a_{\epsilon,i}(\phi_k, \phi_l) = \int_{E^{(i)}} \left(\rho c_p \phi_k \frac{\partial \phi_l}{\partial t} + \nabla \phi_k \cdot (\mathbf{k} \nabla \phi_l) - \rho c_p \phi_k \mathbf{v} \cdot \nabla \phi_l \right) dE^{(i)} \quad (44a)$$

$$\begin{aligned} &= - \sum_{j \in \mathcal{N}_i \cup \{T_b\}} \int_{e_{ij}} \{ \mathbf{k} \nabla \phi_k \cdot n \} [\phi_l] de_{ij} + \epsilon \sum_{j \in \mathcal{N}_i \cup \{T_b\}} \int_{e_{ij}} \{ \mathbf{k} \nabla \phi_l \cdot n \} [\phi_k] de_{ij} \\ &\quad + \sigma \sum_{j \in \mathcal{N}_i \cup \{T_b\}} \int_{e_{ij}} [\phi_k] [\phi_l] de_{ij} \end{aligned} \quad (44b)$$

$$L_i(v) = \epsilon \sum_{j \in \mathcal{N}_i \cup \{T_b\}} \int_{e_{ij}} (\mathbf{k} \nabla \phi_l \cdot n) T_b de_{ij} + \int_{e_{iq}} \phi_k q_b de_{iq} + \sigma \int_{e_{iT}} \phi_k T_b de_{iT} \quad (44c)$$

³⁷⁵ In the bi-linear form above, the notations $[]$ and $\{ \}$ are respectively the jumps and averages
³⁷⁶ at the boundary e_{ij} share by two elements E_i and E_j ,

$$[u] = u|_{E_i} - u|_{E_j}, \quad \{u\} = \frac{1}{2} \left(u|_{E_i} + u|_{E_j} \right), \quad \text{for } x \in e_{ij} = E_i \cap E_j$$

³⁷⁷ Furthermore, in the bi-linear form, the terms associated with σ are introduced to enforce
³⁷⁸ the Dirichlet boundary conditions; σ is a penalty factor whose value can depend on the size
³⁷⁹ of an element. Depending on the choice of ϵ , the bi-linear form corresponds to symmetric
³⁸⁰ IPG ($\epsilon = -1$), non-symmetric IPG ($\epsilon = 1$), and incomplete IPG ($\epsilon = 0$). All these schemes
³⁸¹ are consistent with the original PDE and have similar convergence rate with respect to mesh
³⁸² size. In the following derivations, the case $\epsilon = 0$ is chosen for the sake of simplicity.

³⁸³ **A.1.3 Discontinuous Galerkin Model**

³⁸⁴ Next, the DG-based model is written in an element-wise form. For the i -th element, use a
³⁸⁵ set of P trial functions to represent the temperature as in eq. (6). Without loss of generality,
³⁸⁶ the trial functions are assumed to be orthogonal, so that $\int_{E^{(i)}} \phi_k^{(i)}(x) \phi_l^{(i)}(x) dx = |E^{(i)}| \delta_{kl}$,
³⁸⁷ where $|E^{(i)}|$ is the area ($n_d = 2$) or volume ($n_d = 3$) of the i -th element, and δ_{kl} is the
³⁸⁸ Kronecker delta.

³⁸⁹ Using test functions same as trial functions, the dynamics $\mathbf{u}^{(i)}$ is obtained by evaluating

³⁹⁰ the element-wise bi-linear forms,

$$a_{\epsilon,i}(\phi_k^{(i)}, T^{(i)}) = L_i(\phi_k^{(i)}), \quad k = 1, 2, \dots, P \quad (45)$$

³⁹¹ The above procedure yields,

$$\mathbf{A}^{(i)} \dot{\mathbf{u}}^{(i)} = (\mathbf{B}^{(i)} + \mathbf{C}^{(i)}(t)) \mathbf{u}^{(i)} + \sum_{j \in \mathcal{N}_i \cup \{T_b\}} \left(\mathbf{B}_{ij}^{(i)} \mathbf{u}^{(i)} + \mathbf{B}_{ij}^{(j)} \mathbf{u}^{(j)} \right) + \mathbf{f}^{(i)}(t) \quad (46)$$

³⁹² where for $k, l = 1, 2, \dots, P$,

$$[\mathbf{A}^{(i)}]_{kl} = \int_{E^{(i)}} \rho c_p \phi_k^{(i)} \phi_l^{(i)} dE^{(i)} \quad (47a)$$

$$[\mathbf{B}^{(i)}]_{kl} = - \int_{E^{(i)}} (\nabla \phi_k^{(i)}) \cdot (\mathbf{k} \nabla \phi_l^{(i)}) dE^{(i)} \quad (47b)$$

$$[\mathbf{C}^{(i)}]_{kl} = \int_{E^{(i)}} \rho c_p \phi_k^{(i)} \mathbf{v}^{(i)} \cdot \nabla \phi_l^{(i)} dE^{(i)} \quad (47c)$$

$$[\mathbf{B}_{ij}^{(i)}] = \int_{e_{ij}} \left\{ \mathbf{k} \nabla \phi_k^{(i)} \cdot \hat{n} \right\} \phi_l^{(i)} - \sigma [\phi_k^{(i)}] \phi_l^{(i)} de_{ij} \quad (47d)$$

$$[\mathbf{B}_{ij}^{(j)}] = \int_{e_{ij}} - \left\{ \mathbf{k} \nabla \phi_k^{(i)} \cdot \hat{n} \right\} \phi_l^{(j)} + \sigma [\phi_k^{(i)}] \phi_l^{(j)} de_{ij} \quad (47e)$$

$$[\mathbf{f}^{(i)}]_k = \int_{e_{iq}} \phi_k^{(i)} q_b de_{iq} + \sigma \int_{e_{iT}} \phi_k^{(i)} de_{iT} \quad (47f)$$

³⁹³ The matrices $\mathbf{A}^{(i)} \in \mathbb{R}^{P \times P}$, $\mathbf{B}^{(i)} \in \mathbb{R}^{P \times P}$, and $\mathbf{C}^{(i)} \in \mathbb{R}^{P \times P}$ are respectively the capacitance,
³⁹⁴ conductivity, and advection matrices for element i . These matrices depend on ρ , c_p , \mathbf{k} , and
³⁹⁵ \mathbf{v} , and hence can be non-linear functions of $\mathbf{u}^{(i)}$. Since the trial functions are orthogonal, if
³⁹⁶ ρc_p is constant within an element, $\mathbf{A}^{(i)}$ is diagonal; otherwise, \mathbf{A}_i is symmetric and positive
³⁹⁷ definite as $\rho c_p > 0$.

³⁹⁸ For compactness, the element-wise model in eq. (46) is also written in matrix form,

$$\mathbf{A}(\dot{\mathbf{u}}) = [\mathbf{B}(\mathbf{u}) + \mathbf{C}(\mathbf{u})] \mathbf{u} + \mathbf{f}(t) \quad (48)$$

³⁹⁹ where $\mathbf{u} = [\mathbf{u}^{(1)}, \mathbf{u}^{(2)}, \dots, \mathbf{u}^{(M)}]^T \in \mathbb{R}^{MP}$ includes all DG variables, $\mathbf{f} = [\mathbf{f}^{(1)}, \mathbf{f}^{(2)}, \dots, \mathbf{f}^{(M)}]^T \in \mathbb{R}^{MP}$, \mathbf{A} and \mathbf{C} are matrices of M diagonal blocks whose i -th blocks are $\mathbf{A}^{(i)}$ and $\mathbf{C}^{(i)}$, and
⁴⁰⁰ \mathbf{B} is a matrix of $M \times M$ blocks whose (i, j) -th block is,
⁴⁰¹

$$\mathbf{B}_{ij} = \begin{cases} \mathbf{B}^{(i)} + \sum_{j \in \mathcal{N}_i \cup \{T_b\}} \mathbf{B}_{ij}^{(i)}, & i = j \\ \mathbf{B}_{ij}^{(j)}, & i \neq j \end{cases} \quad (49)$$

402 The dependency of \mathbf{A} , \mathbf{B} , and \mathbf{C} on \mathbf{u} is explicitly noted in eq. (48), which is the source of
403 non-linearity in the current TPS problem. Moreover, the mesh velocity \mathbf{v} varies with space
404 and time, and thus the advection matrix \mathbf{C} varies with time as a function of q_b .

405 A.2 Coarse-Graining of Dynamics

406 The LCM is obtained by coarse-graining the full-order DG-FEM. This coarse-graining proce-
407 dure produces resolved $\mathbf{r}^{(1)}(\mathbf{u}, t)$ and residual $\mathbf{r}^{(2)}(\mathbf{u}, t)$ dynamics as in eq. (23). This section
408 presents the detail derivations and magnitude analysis for the resolved and residual dynam-
409 ics.

410 A.2.1 Resolved Dynamics

411 Using eq. (20), the resolved dynamics is computed as follows,

$$\mathbf{r}^{(1)}(\mathbf{u}, t) = \mathcal{P} [\Phi^+ \mathbf{A}(\mathbf{u})^{-1} (\mathbf{B}(\mathbf{u})\mathbf{u} + \mathbf{C}(\mathbf{u})\mathbf{u} + \mathbf{f}(t))] \quad (50a)$$

$$\begin{aligned} &= \Phi^+ \mathbf{A}(\mathbf{Pu})^{-1} \mathbf{PB}(\mathbf{Pu}) \mathbf{Pu} + \Phi^+ \mathbf{A}(\mathbf{Pu})^{-1} \mathbf{PC}(\mathbf{Pu}) \mathbf{Pu} \\ &\quad + \Phi^+ \mathbf{A}(\mathbf{Pu})^{-1} \mathbf{Pf}(t, \mathbf{Pu}) \end{aligned} \quad (50b)$$

$$\begin{aligned} &= \underbrace{\Phi^+ \mathbf{A}(\Phi \bar{\mathbf{u}})^{-1} \Phi}_{\#1} \underbrace{\Phi^+ \mathbf{B}(\Phi \bar{\mathbf{u}}) \Phi \bar{\mathbf{u}}}_{\#2} + \Phi^+ \mathbf{A}(\Phi \bar{\mathbf{u}})^{-1} \Phi \underbrace{\Phi^+ \mathbf{C}(\Phi \bar{\mathbf{u}}) \Phi \bar{\mathbf{u}}}_{\#3} \\ &\quad + \Phi^+ \mathbf{A}(\Phi \bar{\mathbf{u}})^{-1} \Phi \underbrace{\Phi^+ \mathbf{f}(t, \Phi \bar{\mathbf{u}})}_{\#4} \end{aligned} \quad (50c)$$

412 Detailed derivations for the #1, #2, and #4 terms can be found in Ref. [x](#). The effects of
413 coarse-graining on the advection term #3 are analyzed next.

414 **Term #3** The $\mathbf{C}(\mathbf{u}) \in \mathbb{R}^{MP \times MP}$ matrix contains M diagonal of size $P \times P$, since the
415 basis functions are defined locally on each element. Therefore, $[\mathbf{C}(\mathbf{u})]_{ij} = \mathbf{0}$ for all $i \neq j$ with
416 $i, j = 1, 2, \dots, M$. It follows that for $k, l = 1, 2, \dots, N$,

$$[\Phi^+ \mathbf{C}(t, \Phi \bar{\mathbf{u}}) \Phi]_{kl} = \sum_{i=1}^M \sum_{j=1}^M \boldsymbol{\varphi}_i^{k+} [\mathbf{C}(t, \Phi \bar{\mathbf{u}})]_{ij} \boldsymbol{\varphi}_j^l \quad (51a)$$

$$= \sum_{i=1}^M \boldsymbol{\varphi}_i^{k+} [\mathbf{C}(t, \Phi \bar{\mathbf{u}})]_{ii} \boldsymbol{\varphi}_i^l \quad (51b)$$

$$= \sum_{i \in \mathcal{V}_k} \boldsymbol{\varphi}_i^{k+} [\mathbf{C}(t, \Phi \bar{\mathbf{u}})]_{ii} \boldsymbol{\varphi}_i^l \quad (51c)$$

417 where in the second row, the fact that $[\mathbf{C}(\mathbf{u})]_{ij} = 0$ for all $i \neq j$ is used, and in the last row,
418 the fact that $\varphi_i^{k+} = 0$ for all $i \notin \mathcal{V}_k$ is used. Now, considering that $[\mathbf{C}(\mathbf{u})]_{ii}$ has a $(1, 1)$ -th
419 zero element, i.e., $[C_{11}(t, \Phi\bar{\mathbf{u}})]_{ii} = 0$, and that if $k \neq l$ then $i \notin \mathcal{V}_l$ and thus $\varphi_i^l = \mathbf{0}$, it follows
420 that for some index $i \in \mathcal{V}_k$,

$$\varphi_i^{k+} [\mathbf{C}(t, \Phi\bar{\mathbf{u}})]_{ii} \varphi_i^l = \varphi_i^{k+} [\mathbf{C}(t, \Phi\bar{\mathbf{u}})]_{ii} \varphi_i^k = \frac{|E_i|}{|\Omega_k|} [C_{11}(t, \Phi\bar{\mathbf{u}})]_{ii} = 0 \quad (52)$$

421 The matrix $[\Phi^+ \mathbf{C}(t, \Phi\bar{\mathbf{u}}) \Phi]_{kl} = 0$ for all $k, l = 1, 2, \dots, N$, and thus,

$$\bar{\mathbf{C}}(t, \bar{\mathbf{u}}) = \Phi^+ \mathbf{C}(t, \Phi\bar{\mathbf{u}}) \Phi = \mathbf{0} \quad (53)$$

422 as indicated by the LCM in eq. (9).

423 A.2.2 Magnitude Analysis for Residual Dynamics

424 Next, the magnitude of the residual dynamics $\mathbf{r}^{(2)}(\mathbf{u}, t)$ is analyzed to pinpoint the missing
425 physics in the LCM. By definition,

$$\mathbf{r}^{(2)}(\mathbf{u}, t) = \dot{\bar{\mathbf{u}}} - \mathbf{r}^{(1)}(\bar{\mathbf{u}}, t) \quad (54a)$$

$$= \Phi^+ \mathbf{r}(\mathbf{u}, t) - \mathbf{r}^{(1)}(\mathbf{u}, t) \quad (54b)$$

$$\begin{aligned} &= \underbrace{\Phi^+ \mathbf{A}(\mathbf{u})^{-1} \mathbf{B}(\mathbf{u}) \mathbf{u} - \bar{\mathbf{A}}(\bar{\mathbf{u}})^{-1} \bar{\mathbf{B}}(\bar{\mathbf{u}}) \bar{\mathbf{u}}}_{\#1} + \underbrace{\Phi^+ \mathbf{A}(\mathbf{u})^{-1} \mathbf{C}(\mathbf{u}) \mathbf{u} - \bar{\mathbf{A}}(\bar{\mathbf{u}})^{-1} \bar{\mathbf{C}}(t, \bar{\mathbf{u}}) \bar{\mathbf{u}}}_{\#2} \\ &\quad + \underbrace{\Phi^+ \mathbf{A}(\mathbf{u})^{-1} \mathbf{f}(t) - \bar{\mathbf{A}}(\bar{\mathbf{u}})^{-1} \bar{\mathbf{f}}(t)}_{\#3} \end{aligned} \quad (54c)$$

426 The magnitude analysis for terms $\#1$ and $\#3$ can be found in Ref. [x](#). The analysis for term
427 $\#2$ is presented next. Let $\mathbf{D}(\bar{\mathbf{u}}) = \mathbf{A}(\Phi\bar{\mathbf{u}})^{-1} \mathbf{P} \mathbf{C}(t, \Phi\bar{\mathbf{u}})$, then,

$$\Phi^+ \mathbf{A}(\mathbf{u})^{-1} \mathbf{C}(\mathbf{u}) \mathbf{u} - \bar{\mathbf{A}}(\bar{\mathbf{u}})^{-1} \bar{\mathbf{C}}(t, \bar{\mathbf{u}}) \bar{\mathbf{u}} \quad (55a)$$

$$= \Phi^+ \mathbf{A}(\mathbf{u})^{-1} \mathbf{C}(\mathbf{u}) \mathbf{u} - \Phi^+ \mathbf{A}(\Phi\bar{\mathbf{u}})^{-1} \mathbf{P} \mathbf{C}(t, \Phi\bar{\mathbf{u}}) \Phi \Phi^+ \mathbf{u} \quad (55b)$$

$$= \Phi^+ \mathbf{A}^{-1}(\mathbf{u}) \mathbf{C}(\mathbf{u}) \mathbf{u} - \Phi^+ \mathbf{D}(\bar{\mathbf{u}}) \Phi \Phi^+ \mathbf{u} \quad (55c)$$

$$(55d)$$

⁴²⁸ where $\mathbf{P} = \Phi\Phi^+$. Thus,

$$\|\Phi^+\mathbf{A}(\mathbf{u})^{-1}\mathbf{C}(\mathbf{u})\mathbf{u} - \bar{\mathbf{A}}^{-1}(\bar{\mathbf{u}})\bar{\mathbf{C}}(t, \bar{\mathbf{u}})\bar{\mathbf{u}}\| \quad (56a)$$

$$\leq \|\Phi^+\mathbf{A}^{-1}(\mathbf{u})\mathbf{C}(\mathbf{u})\mathbf{u} - \Phi^+\mathbf{D}(\bar{\mathbf{u}})\mathbf{u}\| + \|\Phi^+\mathbf{D}(\bar{\mathbf{u}})\mathbf{u} - \Phi^+\mathbf{D}(\bar{\mathbf{u}})\Phi\Phi^+\mathbf{u}\| \quad (56b)$$

$$\leq \|\Phi^+\| \underbrace{\|\mathbf{A}^{-1}(\mathbf{u})\mathbf{C}(\mathbf{u})\mathbf{u} - \mathbf{D}(\bar{\mathbf{u}})\mathbf{u}\|}_{\#1} + \|\Phi^+\mathbf{D}(\bar{\mathbf{u}})\| \underbrace{\|\mathbf{u} - \Phi\Phi^+\mathbf{u}\|}_{\#2} \quad (56c)$$

⁴²⁹ where term $\#2$ is due to the approximation of non-uniform temperature as constants, and
⁴³⁰ term $\#1$ is the error in the advection dynamics due to coarse-graining.

⁴³¹ A.3 Lumped Capacitance Model

⁴³² The following assumptions are employed: (1) the temperature in component (i) is described
⁴³³ by a scalar time-varying average temperature $\bar{u}^{(i)}$, (2) between neighboring components (i)
⁴³⁴ and (j) the heat flux is approximated as,

$$q_{ij} = \frac{\bar{u}^{(j)} - \bar{u}^{(i)}}{R_{ij}} \quad (57)$$

⁴³⁵ where R_{ij} is the thermal resistance. Empirically, for a component of isotropic heat conduction
⁴³⁶ conductivity k , length ℓ , and cross-section area A , the thermal resistance is $R = \ell/kA$. Between
⁴³⁷ components i and j , define $R_{ij} = R_i + R_j$. In addition, the heat flux due to Dirichlet
⁴³⁸ boundary condition is computed as $q_{iT} = (T_b - \bar{u}^{(i)})/R_i$.

⁴³⁹ At component i , the dynamics of LCM are given by,

$$\int_{E^{(i)}} \rho c_p \dot{\bar{u}}^{(i)} dE^{(i)} = \left(\sum_{j \in \mathcal{N}_i} \int_{e_{ij}} \frac{\bar{u}^{(j)} - \bar{u}^{(i)}}{R_{ij}} de_{ij} \right) + \int_{e_{iq}} q_b de_{iq} + \int_{e_{iT}} \frac{T_b - \bar{u}^{(i)}}{R_i} de_{iT} \quad (58a)$$

$$\bar{A}^{(i)} \dot{\bar{u}}^{(i)} = \left(\sum_{j \in \mathcal{N}_i} \frac{|e_{ij}|}{R_{ij}} (\bar{u}^{(j)} - \bar{u}^{(i)}) \right) + |e_{iq}| \bar{q}^{(i)} + \frac{|e_{iT}|}{R_i} (\bar{T}^{(i)} - \bar{u}^{(i)}) \quad (58b)$$

$$= \sum_{j \in \mathcal{N}_i} \left(-\frac{|e_{ij}|}{R_{ij}} \bar{u}^{(i)} + \frac{|e_{ij}|}{R_{ij}} \bar{u}^{(j)} \right) + \left(-\frac{|e_{iT}|}{R_i} \bar{u}^{(i)} \right) + \left(|e_{iq}| \bar{q}^{(i)} + \frac{|e_{iT}|}{R_i} \bar{T}^{(i)} \right) \quad (58c)$$

$$= \sum_{j \in \mathcal{N}_i \cup \{T_b\}} \left(\bar{B}_{ij}^{(i)} \bar{u}^{(i)} + \bar{B}_{ij}^{(j)} \bar{u}^{(j)} \right) + \bar{f}^{(i)} \quad (58d)$$

⁴⁴⁰ where in eq. (58b) $|e|$ denotes the length ($d = 2$) or area ($d = 3$) of a component boundary
⁴⁴¹ e . The $\bar{A}^{(i)}$, $\bar{B}_{ij}^{(i)}$, and $\bar{B}_{ij}^{(j)}$ quantities are provided in eq. (12).

⁴⁴² The lumped-mass representation for the four-component TPS is shown in Fig. 2. Let v_i

⁴⁴³ represent the area of the i -th element, $\overline{\rho c_p}_i$, the heat capacity evaluated using the average
⁴⁴⁴ temperature $\bar{u}^{(i)}$, and $1/R_{ij} = 1/R_i(\bar{u}^{(i)}) + 1/R_j(\bar{u}^{(j)})$ the equivalent thermal resistance
⁴⁴⁵ between elements i and j . Leveraging the formulas from eqs. (11) and (12), the LCM
⁴⁴⁶ matrices are given by,

$$\bar{\mathbf{A}} = \begin{bmatrix} \overline{\rho c_p}_1 v_1 & 0 & 0 & 0 \\ 0 & \overline{\rho c_p}_2 v_2 & 0 & 0 \\ 0 & 0 & \overline{\rho c_p}_3 v_3 & 0 \\ 0 & 0 & 0 & \overline{\rho c_p}_4 v_4 \end{bmatrix}, \quad (59a)$$

$$\bar{\mathbf{B}} = \begin{bmatrix} \frac{1}{R_{12}} + \frac{1}{R_{14}} & -\frac{1}{R_{12}} & 0 & -\frac{1}{R_{14}} \\ -\frac{1}{R_{12}} & \frac{1}{R_{12}} + \frac{1}{R_{24}} + \frac{1}{R_{23}} & -\frac{1}{R_{23}} & -\frac{1}{R_{24}} \\ 0 & -\frac{1}{R_{32}} & \frac{1}{R_{32}} + \frac{1}{R_{34}} & -\frac{1}{R_{34}} \\ -\frac{1}{R_{14}} & -\frac{1}{R_{24}} & -\frac{1}{R_{34}} & \frac{1}{R_{14}} + \frac{1}{R_{24}} + \frac{1}{R_{34}} \end{bmatrix}, \quad \bar{\mathbf{f}} = \begin{bmatrix} \bar{q}^{(1)} \\ \bar{q}^{(2)} \\ \bar{q}^{(3)} \\ 0 \end{bmatrix} \quad (59b)$$

⁴⁴⁷ References

- ⁴⁴⁸ [1] Adam J. Amar, A. Brandon Oliver, Benjamin S. Kirk, Giovanni Salazar, and Justin Dobra. Overview of the charring ablator response (char) code. In AIAA, editor, *AIAA Aviation Forum*, 2016.
- ⁴⁵¹ [2] Guy L. Bergel, Frank B. Beckwith, Gabriel J. de Frias, Kevin M. Manktelow, Mark T. Merewether, Scott T. Miller, Krishen J. Parmar, Timothy S. Shelton, Jesse T. Thomas, Jeremy T. Trageser, Benjamin T. Treweek, Michael V. Veilleux, and Ellen B. Wagman. *Sierra/SolidMechanics 5.6 User's Manual*, 2022.
- ⁴⁵⁵ [3] Gary Cohen and Sébastien Pernet. *Finite Element and Discontinuous Galerkin Methods for Transient Wave Equations*. Springer Dordrecht, Le Chesnay and Toulouse France, 2018.
- ⁴⁵⁸ [4] Frank P. Incropera, David P. DeWitt, Theodore L. Bergman, and Adrienne S. Lavine. *Fundamentals of Heat and Mass Transfer*. Wiley, Hoboken, NJ, 7th edition, 2011.
- ⁴⁶⁰ [5] Eric Parish and Karthik Duraisamy. Non-markovian closure models for large eddy simulations using the mori-zwanzig formalism. *Phys. Rev. Fluids*, 2:014604, Jan 2017.
- ⁴⁶² [6] Eric Parish and Karthik Duraisamy. A unified framework for multiscale modeling using the mori-zwanzig formalism and the variational multiscale method. *ArXiv*, 12 2017.
- ⁴⁶⁴ [7] Eric Parish and Karthik Duraisamy. *Coarse-Graining Turbulence Using the Mori-Zwanzig Formalism*. Cambridge University Press, Cambridge, 2025.

- 466 [8] Carlos A. Vargas Venegas, Daning Huang, Patrick Blonigan, and John Tencer. Physics-
467 infused reduced-order modeling for analysis of multi-layered hypersonic thermal protec-
468 tion systems. *ArXiv*, 2025.
- 469 [9] Yin Yu, John Harlim, Daning Huang, and Yan Li. Learning coarse-grained dynamics on
470 graph. *arXiv preprint arXiv:2405.09324*, 2024.